Research Square

Preprints are preliminary reports that have not undergone peer review.
They should not be considered conclusive, used to inform clinical practice,
or referenced by the media as validated information.

Influence of Water Vapor on Hot Corrosion @900°C: Nickel-Base Superalloys CMSX-4, Rene 80 and IN939

Julian P. Zander
DECHEMA-Forschungsinstitut
Ceyhun Oskay
DECHEMA-Forschungsinstitut
Lisa Zander
DECHEMA-Forschungsinstitut
Till König
DECHEMA-Forschungsinstitut
Mathias Christian Galetz
mathias.galetz@dechema.de
DECHEMA-Forschungsinstitut

Research Article

Keywords: nickel-base superalloys, CMSX-4, Rene 80, IN939, hot corrosion, water vapor, sulfate deposits, SO_2, K_2SO_4–Na_2SO_4

Posted Date: November 25th, 2026

DOI: https://doi.org/10.21203/rs.3.rs-11649950/v1

License: This work is licensed under a Creative Commons Attribution 4.0 International License.
Read Full License

Additional Declarations: No competing interests reported.

Influence of Water Vapor on Hot Corrosion @900°C: Nickel-Base Superalloys CMSX-4, Rene 80 and IN939

Authors

Julian P. Zander[1], Ceyhun Oskay[1],Lisa Zander[1], Till König[1], Mathias C. Galetz[1]

[1]DECHEMA Research Institute

Abstract

Deposit-induced hot corrosion of the nickel-base superalloys CMSX-4, Rene 80 and IN939 was investigated at 900 °C in an SO_2-containing atmosphere (0.15 %) with repeated application of a K_2SO_4–Na_2SO_4 (80:20, 1.5 µg cm^{-2} h^{-1}) salt mixture. The focus of the study was the influence of water vapor on corrosion mechanisms and kinetics, with H_2O contents of 0, 4 and 20 vol.%. Salt was reapplied every 100 h, and corrosion damage was assessed after exposures of up to 1000 h using cross-sectional analysis, WDX measurements and cumulative probability plots.

The results reveal a strong, alloy-specific effect of water vapor on the hot corrosion attack. CMSX-4 shows severe hot corrosion in dry atmospheres, characterized by mixed oxide scales, internal sulfidation and nitridation. Increasing water-vapor content dramatically reduces corrosion damage and promotes the formation of thin, homogeneous, aluminum-rich oxide scales, with the lowest attack observed at 20 % H_2O. Rene 80 exhibits a complex response to water vapor: moderate H_2O content helps suppressing hot corrosion and prevents molybdate formation, whereas higher H_2O levels lead to increased attack associated with porous chromia and non-protective alumina. In contrast, IN939 shows a corrosion behavior largely independent of water-vapor content, maintaining a continuous chromia-based oxide scale due to its high chromium content.

Cumulative probability analysis confirms that water vapor can significantly mitigate hot corrosion damage, e.g. by stabilizing aluminum-rich protective oxides. The findings demonstrate that the role of water vapor in sulfate-induced hot corrosion is composition dependent and must be considered on an alloy-specific basis for high-temperature turbine applications.

Keywords

nickel-base superalloys; CMSX-4; Rene 80; IN939; hot corrosion; water vapor; sulfate deposits; SO_2; K_2SO_4–Na_2SO_4

1. Introduction

Nickel-based superalloys remain the benchmark for structural components exposed to extreme temperatures (>700 °C) in gas turbine environments. Their success arises from a unique combination of properties, including a high strength-to-density ratio, adequate oxidation resistance, and exceptional creep resistance at elevated temperatures, while their close-packed face-centered cubic (FCC) crystal structure ensures sufficient ductility at lower temperatures. As a result, these alloys have proven difficult to replace in demanding turbine applications .

In pursuit of higher efficiency and lower environmental impact, industrial gas turbine technology has to evolve . These objectives drive operation toward increasingly demanding conditions, including elevated turbine inlet temperatures and the non-conventional fuel compositions . Altered fuel chemistry influences the composition of the flue gas. Hydrogen-rich fuels can substantially increase water vapor concentrations in the hot gas path of the gas turbine approaching 20 vol.% H_2O for the combustion of hydrogen-based or syngas fuels .

The effect of water vapor on high temperature oxidation of chromia forming alloys was studied in several publications . Water vapor was related to an increase in oxidation rates and higher material volatilization due to the formation of volatile species such as $CrO_2(OH)_2$. However there have also been reports on beneficial effects of water vapor like the inhibition of internal nitridation that was observed e.g. for pure chromium . For alumina formers, especially at lower temperatures (~700°C), water vapor weakens reducing selective aluminum oxidation in Ni-base superalloys, causing more transient oxides like NiO to form . It also promotes cracking and spallation of the alumina scale, with the effect being severe for alloys with weak oxide/alloy adhesion but minimal for strongly adherent or platinum-modified coatings .

One highly relevant aspect for structural materials used in gas turbines is deposit induced corrosion. In turbines a major contributor to this phenomenon is sodium sulfate (Na_2SO_4) forming a deposit on the structural materials, upon the reaction of sodium chloride from marine environments with oxygen and sulfur trioxide (SO_3) stemming from impurities in the combusted fuel (or potentially also the environment in case of human or volcanic activity). This accelerated corrosion type is called hot corrosion and is a well described process for Ni-based materials usually subdivided into type I, relevant at temperatures around 900°C and type II occurring around 700°C. Type II is characterized by pitting-like attack due to local formation of $NiSO_4$ or $CoSO_4$ forming a low melting eutectic with Na_2SO_4 . Type I usually shows a more uniform attack due to the fully molten Na_2SO_4 deposit (T_m=884°C). The influence of alloying elements plays a major role in the attack mechanism during hot corrosion. Their transient oxides can dissolve in the salt deposit and influence its acidity . Especially molybdenum (Mo) has been observed to induce strong acidic fluxing by the formation of molybdates . This can even lead to a shift to lower temperatures of the hot corrosion attack .

Potter et al. studied hot corrosion of the Ni-based superalloy PWA 1483 and the Co-based superalloy MarM 509 at 700 °C using a Na_2SO_4–K_2SO_4 deposit, with water vapor levels of 0, 10, and 20 vol.% H_2O in SO_2-containing atmospheres. They found that increasing water vapor reduced metal loss at high SO_2 (300 ppm) but increased metal loss at low SO_2 (3.6 ppm). This shows that at high SO_2 (300 ppm), corrosion is dominated by gas-phase (acidic) fluxing, and increasing water vapor suppresses this by altering sulfur chemistry (e.g. reducing effective sulfur activity and slowing down sulphate decomposition), which lowers the metal loss. At low SO_2 (3.6 ppm), alloy-induced (basic) fluxing becomes dominant. Added water vapor promotes dissolution of protective oxides and refractory-metal phases into the molten salt, increasing metal loss—particularly in alloys rich in refractory elements.

The present study examines how water vapor modifies the high temperature hot corrosion type I for three widely used nickel-base superalloys: CMSX-4 (low Cr, high Al), Rene 80 (intermediate Cr and Al), and IN939 (high Cr). Their differing chromium/aluminum content provides a solid basis to study water-vapor effects at 900 °C (Hot Corrosion Type 1) under molten-sulfate exposure. For this purpose,

synthetic K_2SO_4–Na_2SO_4 (80:20 wt.%) mixtures were deposited on the alloys, recoated multiple times (keeping a flux of 1.5 µg cm^{-2} h^{-1}) and exposed under synthetic air + 0.15 vol.% SO_2 gas mixture and the addition of 0, 4 and 20 vol.% H_2O. While 0 vol% H_2O-vapour reflects the fully dry conditions (which doesn't occur in actual systems but represents many tab tests), 4vol.% H_2O-vapour is the baseline, that reflects current engine operation better and 20vol.% H_2O, which may result from combustion of future hydrogen-rich fuels.

2. Materials and Methods

2.1 Alloys

	Ni	Cr	Al	Co	Mo	Ti	W
CMSX-4	Bal.	11	5.5	10	1.5	1.5	2.5
Rene80	Bal.	14	3	10	4	5	4
IN939	Bal.	22.5	2	20	-	3.8	2

Tabel 1: Elemental contents of the materials used in wt.%.

Three commercial nickel-base superalloys were investigated in this study. Their chemical compositions are summarized in Tabel 1. CMSX-4 is a single-crystal superalloy with low chromium content and high concentrations of aluminum and refractory elements. Rene 80 is a cast polycrystalline alloy with intermediate chromium content and significant additions of aluminum, titanium and molybdenum. IN939 is a polycrystalline cast alloy with high chromium content, specifically designed for oxidation resistance at elevated temperatures.

Prior to exposure, all specimens were ground to 800 grit using a SiC grinding sequence to ensure reproducible and comparable surface conditions for all alloys.

2.2 Salt Mixture and Application

A synthetic sulfate deposit consisting of K_2SO_4–Na_2SO_4 in an 80:20 wt.% ratio was prepared from high-purity salts. To ensure a constant sulfate supply and to avoid salt-depletion effects during long-term exposure, the specimens were periodically removed from the furnace every 100 h. At these intervals, the samples were cooled in ambient air, re-sprayed with the salt suspension, dryed and subsequently reintroduced into the exposure chamber. To achieve a salt deposition flux of 1.5 µg cm^{-2} h^{-1}.

Specimens were collected for detailed metallographic analysis after total exposure times of 200 h, 600 h and 1000 h. Because the samples were repeatedly removed from the furnace for salt reapplication, mass-change measurements cannot provide meaningful information under these conditions and were disregarded.

2.3 Corrosion Environment

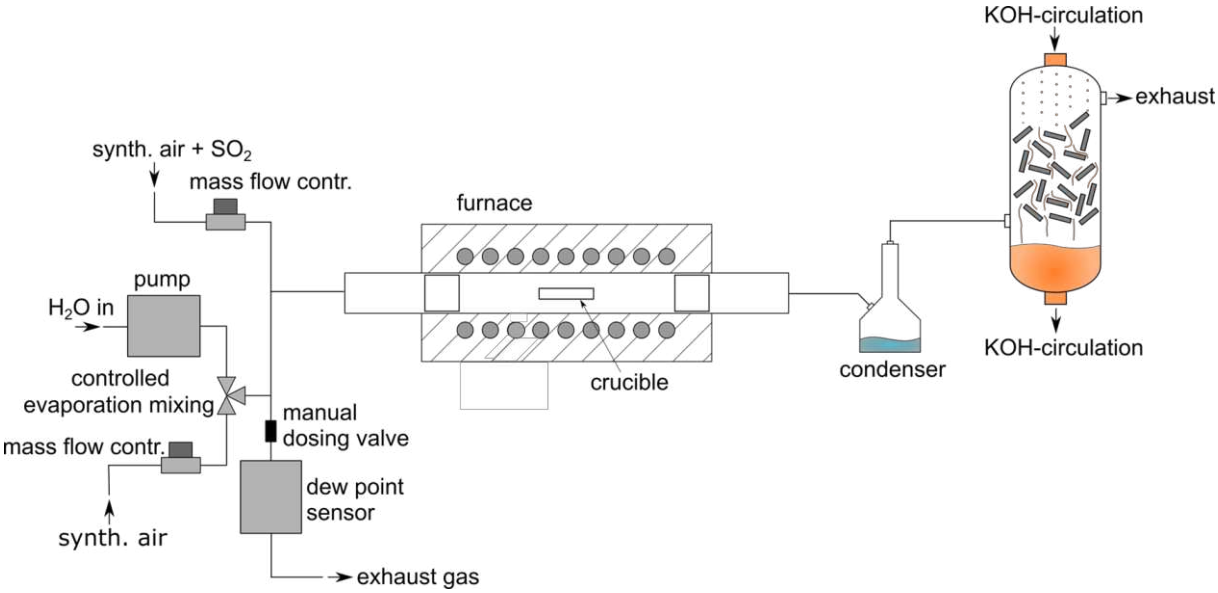

Figure 1: Schematic setup for the hot corrosion experiments with extra water vapor atmosphere.

Hot-corrosion exposures were carried out at 900 °C in a controlled gas atmosphere containing 0.15 vol.% SO_2. Water vapor was added to the gas stream at three different levels: 0 %, 4 % and 20 % (vol.%). A schematic of the experimental setup is shown in, Figure 1.

Gas compositions were regulated using mass-flow controllers and water vapor content was calibrated using a dew point sensor. The water vapor was introduced via a dedicated steam-injection system consisting of a calibrated water pump (Wadose Flusys GmbH) and an evaporation unit. The total gas flow rate was kept constant for all experiments to ensure comparability between exposure conditions. After exposure times of 200 h, 600 h and 1000 h, the specimens were removed for microstructural characterization.

2.4 Characterization

After exposure, all specimens were cold-mounted, sectioned perpendicular to the exposed surface and prepared using metallographic polishing in petroleum down to sub-micron diamond suspensions. This preparation enabled reproducible assessment of oxide scale thickness, internal sulfidation depth, chromium and aluminum depletion zones, and metal loss.

Microstructural characterization was performed using scanning electron microscopy (SEM) to examine the degradation and morphology of oxides and sulfides. High-resolution compositional analysis was carried out by wavelength-dispersive X-ray spectroscopy (WDX, ESMA) to obtain detailed elemental distributions of Cr, Al, Mo, S, O and other alloying elements. WDX analyses were performed for all exposure times (200 h, 600 h and 1000 h) and all water-vapor levels to identify chromate-, molybdate- and sulfate-derived reaction zones and to quantify compositional gradients.

Corrosion damage was quantified by measuring external oxide scale thicknesses, internal degradation zones resulting from sulfidation and oxide penetration, and the effective metal loss derived from cross-sectional profiles. By continuously measuring of the whole relevant areas of the specimen (except those close to edges) using the software Imagic and sorting the data, cumulative probability plots of the material loss were derived. To obtain these plots, light microscopic overlapping images with a ×100 magnification were taken along the entire surface and subsequently stitched together. This

methodology provides a mechanistically robust evaluation of corrosion attack and degradation morphology in order to generate cumulative probability analysis .

3. Results and Discussion

Figure 2. gives an overview of the microstructural evolution of the exposed CMSX-4, Rene 80 and IN939 (pls. note the different scale bars). This microstructural evolution depends strongly on the alloy. For CMSX-4 high degradation rates are observed for tests with 0 % H_2O after all exposure times, whereas with increasing H_2O-content the hot corrosion attack decreases and a protective oxide scale is formed (detailed analysis in the following section). On the contrary, Rene 80 shows the lowest hot corrosion attack in the exposure with 4 % H_2O. With 20 % H_2O the attack on Rene 80 increases. The degradation of IN939 is independent of the H_2O-content low.

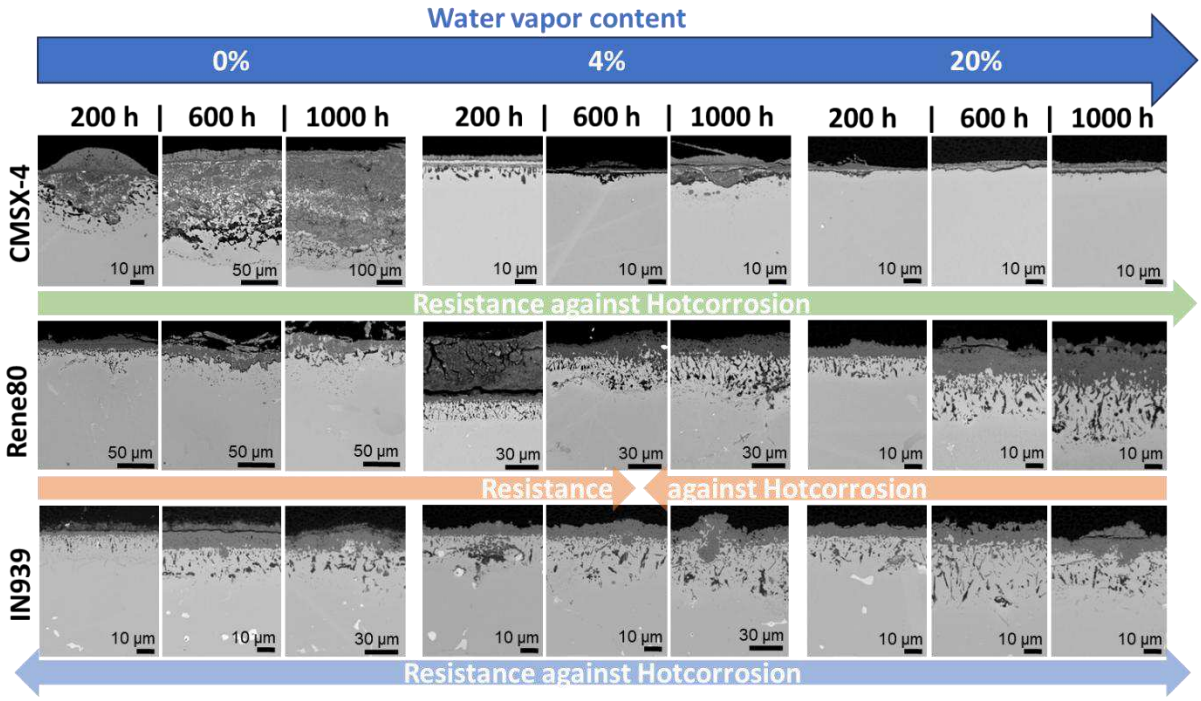

Figure 1. Overview of the hot corrosion behavior of investigated alloys at every water content (0, 4, 20 vol.%) and exposure time (200, 600, 1000 h). Consider different scale bars and some of the samples showed severe spallation.

3.1 Effect of Water Vapor (0 vs. 4 vs. 20 % H_2O) at 1000 h

3.1.1 CMSX-4

After 1000 h of exposure under deposit-induced hot-corrosion conditions, CMSX-4 exhibits a pronounced and systematic dependence of degradation behavior on the water-vapor content of the atmosphere.

CMSX4 at 0% H2O:

In the absence of water vapor, CMSX-4 suffers severe hot-corrosion attack [20,21]. Cross-sectional analysis shows that no continuous or protective Al_2O_3 layer is established. Instead, a thick, non-protective mixed oxide scale forms at the surface, Figure 3, and in some cases strong pitting occurs, Figure 4. WDX measurements identify this scale as a heterogeneous mixture dominated by Al-, Cr- and

Co-oxides, with additional contributions from Ni-, Ti- and Ta-oxides. The intimate intermixing of these oxides indicates repeated scale breakdown and re-formation rather than controlled, diffusion-limited growth. Beneath the external scale, internal degradation is extensive. WDX maps reveal finely dispersed sulfur-containing species, homogeneously distributed within the alloy near the corrosion front, consistent with sulfate-induced sulfidation following oxide destabilization. In addition, internal aluminum nitrides are present, indicating locally high nitrogen activity once protective oxide formation is suppressed. The coexistence of internal sulfidation and nitride formation demonstrates that CMSX-4 remains chemically unprotected throughout the exposure under dry conditions.

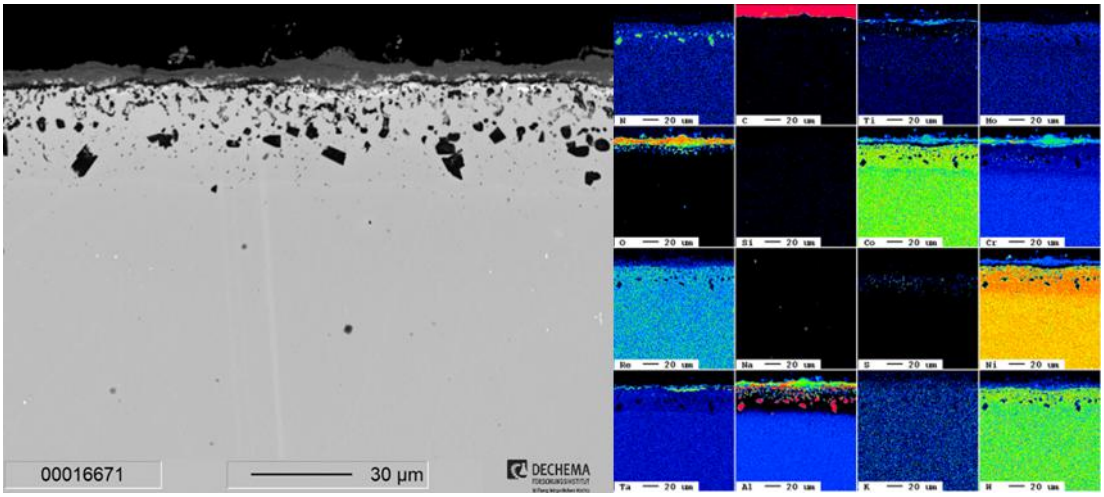

Figure 3: Cross-sectional BSE image and elemental distribution maps for CMSX-4 after hot corrosion without water vapor at 900°C for 1000 h – zone without pit.

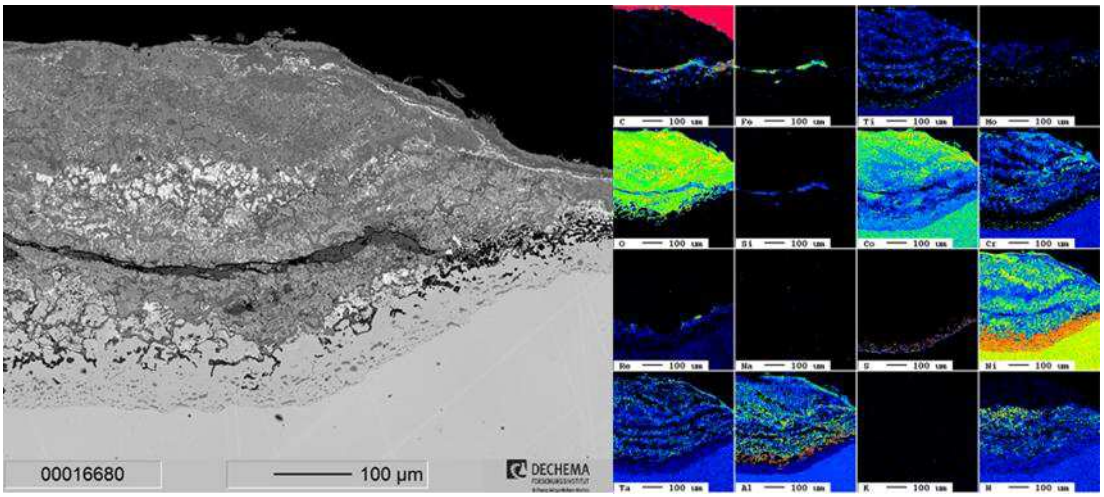

Figure 4: Cross-sectional BSE image and elemental distribution maps for CMSX-4 after hot corrosion without water vapor at 900°C for 1000 h – zone with pit.

CMSX4 at 4% H2O:

The introduction of 4 % H_2O results in a dramatic reduction of corrosion damage. Cross-sections show a substantially thinner and more uniform oxide scale compared to the dry condition, Figure 5. In contrast to the mixed oxide observed at 0 % H_2O, the scale now exhibits a clearly layered structure. WDX analysis reveals a reproducible compositional sequence from the alloy toward the surface:

Al → Ti → Ta → Cr → Ni

This hierarchy of layers indicates selective oxidation and element-specific transport under quasi-steady-state conditions. Cobalt oxide does not form a discrete layer but is primarily incorporated within the Ni-rich outer oxide and locally within the Al-rich inner oxide, while being largely absent from the intermediate Ti-, Ta- and Cr-dominated layers. Importantly, no sulfur-containing species are detected, particularly within the alloy substrate, indicating effective suppression of sulfidation processes. Internal aluminum nitrides are still present, but their extent is reduced compared to the dry condition. Overall, the corrosion morphology at 4 % H_2O is characteristic of a system that, while not forming a fully continuous alumina scale, has transitioned to a far more controlled and chemically differentiated oxidation mechanism.

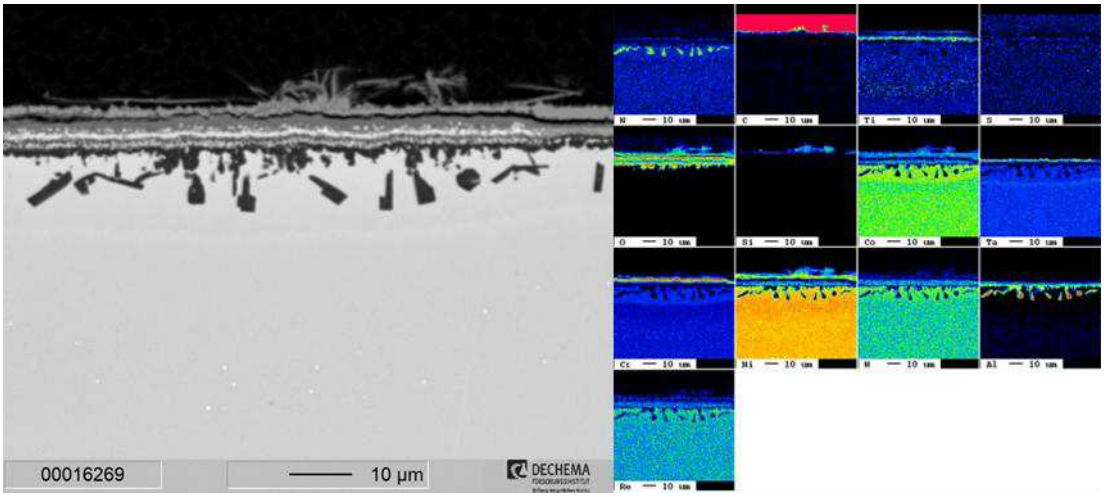

Figure 5: Cross-sectional BSE image and elemental distribution maps for CMSX-4 after hot corrosion exposure of CMSX-4 with 4% water vapor at 900°C for 1000 h.

CMSX4 at 20% H2O:

At 20 % H_2O, the corrosion attack is further reduced, representing the most protective condition observed for CMSX-4 after 1000 h. The oxide scale remains layered but is significantly thinner than at 4 % H_2O, Figure 6. In addition to the previously observed sequence, WDX measurements reveal the formation of a tungsten-rich oxide layer located above the Al-rich inner oxide. Internal aluminum nitride formation is strongly suppressed, and no sulfur-containing species are detected within the alloy. The combination of reduced scale thickness, suppressed internal reactions and well-defined layering indicates that high water-vapor contents fundamentally alter the interfacial chemistry in a way that stabilizes oxidation and inhibits sulfate-driven degradation.

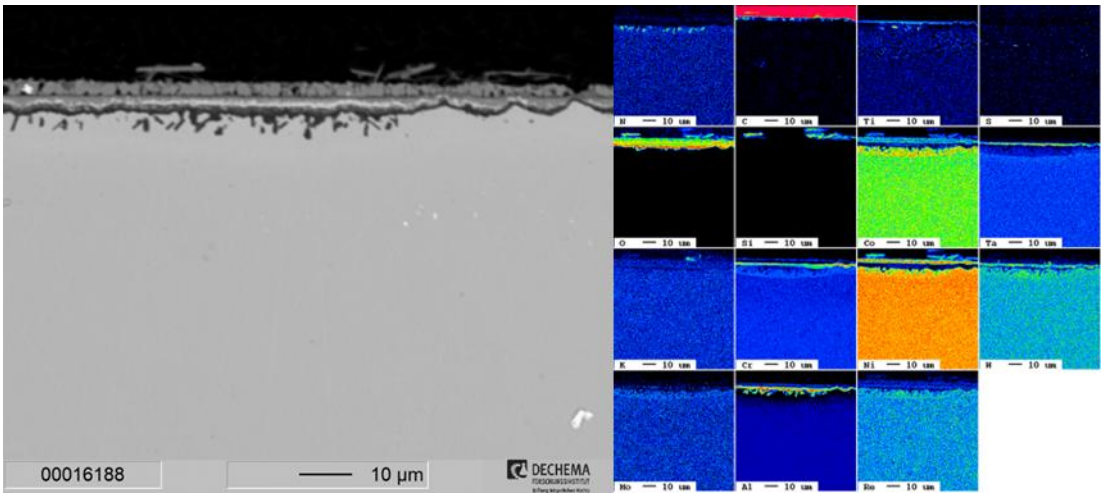

Figure 6: Cross-sectional BSE image and elemental distribution maps for CMSX-4 after hot corrosion exposure with 20% water vapor at 900°C for 1000 h.

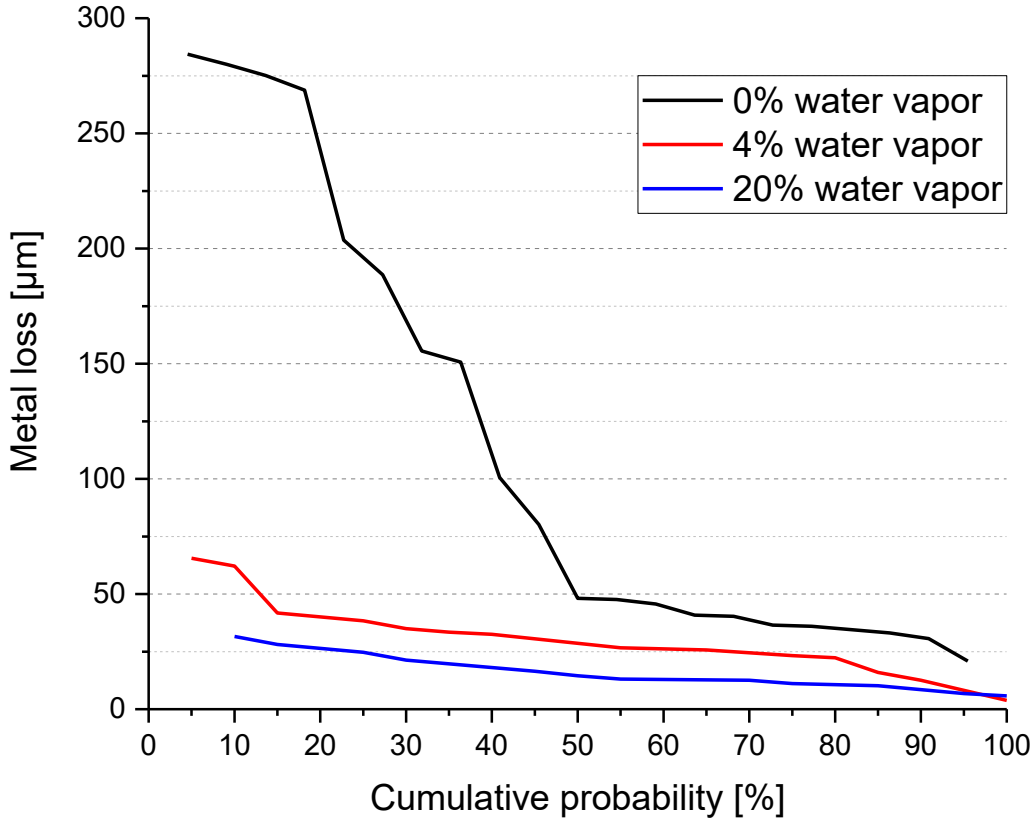

Figure 7: Cumulative probability plot for remaining intact metal: CMSX-4 hot corrosion experiments with 0, 4 and 20% water vapor.

The trends observed in the WDX measurements are fully corroborated by the cumulative probability plots of the remaining intact alloy cross-section, Figure 7. At 0 % H_2O, CMSX-4 exhibits the most severe material loss. The cumulative distribution shows pronounced scatter and the presence of localized pitting, with maximum attack depths reaching up to ~300 µm. The median value indicates that 50 % of the measured cross-sections experience an attack depth of approximately 50 µm, reflecting both high average degradation and strong spatial variability. The addition of 4 % H_2O leads to a marked improvement. The cumulative plot shifts toward lower attack depths, and no pitting is observed. The median attack depth is reduced to approximately 30 µm, indicating a transition from localized, aggressive attack to more uniform and limited degradation. At 20 % H_2O, CMSX-4 shows the highest

resistance against hot corrosion. The cumulative distribution is narrow, no pits are detected, and 50 % of the remaining metal measurements exhibit an attack depth of only ~15 µm after 1000 h. This confirms that increasing water-vapor content systematically enhances the effective protection of CMSX-4 under the investigated conditions.

The CMSX-4 results demonstrate a clear, monotonic increase in corrosion resistance with increasing water-vapor content, as evidenced by both microstructural analysis and statistical evaluation of metal loss. Under dry conditions, molten sulfate deposits promote extensive oxide dissolution, sulfidation and internal nitride formation, preventing the establishment of any protective barrier. The introduction of water vapor fundamentally alters this behavior. Moderate H_2O levels (4 %) suppress sulfidation and promote chemically stratified oxide growth, while high H_2O levels (20 %) further stabilize the oxide scale and significantly reduce internal reactions. This behavior can be rationalized by water-vapor-induced changes in sulfate melt chemistry and gas-phase equilibria. Increased H_2O modifies the SO_2/SO_3 balance and the acid–base characteristics of the molten sulfate, reducing the chemical driving force for aggressive oxide dissolution and sulfur ingress. For a low-Cr, Al-rich superalloy such as CMSX-4, these changes are sufficient to shift the dominant degradation mechanism from continuous hot corrosion toward a more controlled oxidation regime, even though a fully continuous alumina scale is not formed.

Overall, CMSX-4 exhibits a strongly beneficial response to increasing water-vapor content under deposit-induced hot-corrosion conditions at 900 °C, highlighting that humidity can act as a stabilizing parameter rather than an accelerating factor for certain nickel-base superalloys.

3.1.2 Rene80

After 1000 h of exposure under deposit-induced hot-corrosion conditions, Rene 80 exhibits a strong dependence of corrosion behavior on the water-vapor content of the atmosphere. Compared to CMSX-4, the degradation mechanisms are dominated by chromia instability and molybdenum-assisted hot corrosion.

Rene80 at 0% H2O:

In the absence of water vapor, Rene 80 suffers severe hot-corrosion attack, as reported before by different authors [22,23]. Cross-sectional analysis reveals extensive surface degradation and deep penetration of corrosion products into the alloy, Figure 8. WDX measurements show a pronounced sulfur attack, with sulfur-rich regions extending far beneath the external scale. In contrast to CMSX-4, no internal nitridation is observed under these conditions. The external oxide scale is highly discontinuous, consisting of fragmented and chemically heterogeneous Al- and Cr-rich oxides. These oxides do not form a coherent protective barrier and are repeatedly disrupted by ongoing corrosion reactions. Above the residual oxide, molybdate-rich phases are detected, indicating the formation of alkali molybdates in the sulfate deposit. This observation is characteristic of an advanced propagation stage of hot corrosion, where Mo actively participates in scale dissolution and sulfur transport. Minor amounts of Ni-, Co- and Ti-oxides are present, but they do not contribute to scale integrity. The dominant oxide sequence, where distinguishable, follows the order:

Al → Cr → Ti → Mo

from the alloy toward the surface. Overall, the surface morphology appears severely disrupted and irregular, reflecting uncontrolled oxide breakdown and sustained sulfate-driven attack.

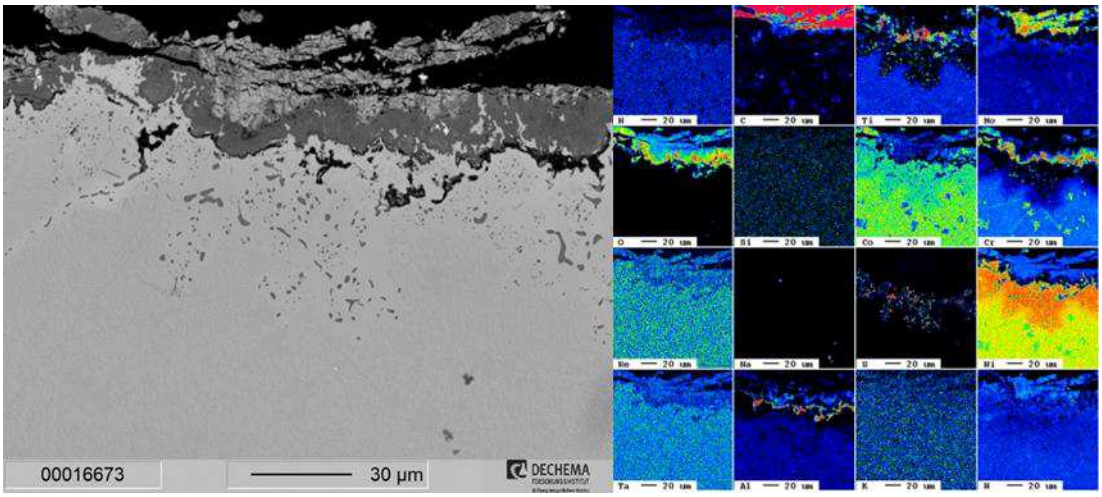

Figure 8: Cross-sectional BSE image and elemental distribution maps for Rene80 after hot corrosion without water vapor at 900°C for 1000 h.

Rene80 at 4% H2O:

At 4 % H_2O, the corrosion behavior of Rene 80 changes fundamentally. Cross-sections reveal a clearly developed oxide scale with significantly reduced overall damage compared to the dry condition, Figure 9. The hot-corrosion attack is strongly suppressed.

WDX analysis shows a small amount of internal aluminum nitrides, indicating limited nitrogen uptake under these conditions. Internal sulfidation is still present but occurs primarily in regions correlated with elevated titanium concentrations, suggesting Ti-assisted sulfur transport. Beneath the surface, an internal aluminum-depleted zone is observed, above which an internal, discontinuous Al-rich oxide forms. Between these features, regions enriched in Ni and Co, as well as W, Ta and Re, are detected, while titanium is largely absent from this internal zone.

The external oxide scale exhibits a layered structure. The outermost layer consists predominantly of Ti- and Ni-oxides, beneath which a thick and porous Cr-rich oxide layer develops. A pronounced chromium-depleted zone is present directly beneath the Cr-rich scale, consistent with sustained Cr outward diffusion.

Notably, no molybdate formation is detected under these conditions, indicating that the chemical environment no longer favors Mo participation in sulfate-driven corrosion. Overall, 4 % H_2O leads to a stable corrosion morphology characterized by suppressed sulfidation and controlled oxide growth.

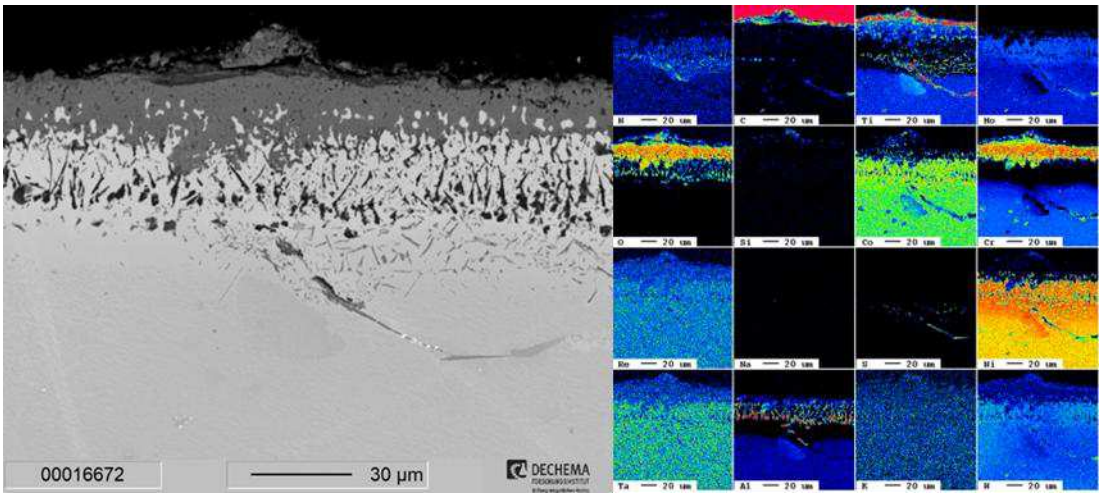

Figure 9: Cross-sectional BSE image and elemental distribution maps for Rene80 after hot corrosion with 4% water vapor at 900 °C for 1000 h.

Rene80 at 20% H2O:

At 20 % H_2O, hot-corrosion attack remains strongly suppressed compared to the dry condition; however, the degradation is more pronounced than at 4 % H_2O. The internal corrosion morphology closely resembles that observed at 4 % H_2O, including limited sulfidation and internal Al depletion, but the surface oxide morphology differs markedly, Figure 10. The external scale consists of nearly spherical, discrete oxide regions composed primarily of Ti-, Cr- and Co-oxides, coexisting side-by-side rather than forming continuous layers. This morphology contrasts with the layered oxide structure observed at 4 % H_2O and indicates a change in oxide nucleation and growth behavior. As at 4 % H_2O, no molybdate phases are detected. The altered oxide morphology suggests that higher water-vapor content modifies oxide growth kinetics, potentially affecting cation transport and local oxidation rates. While the corrosion attack remains significantly lower than in the dry atmosphere, the surface scale is less effective than at 4 % H_2O in limiting further degradation.

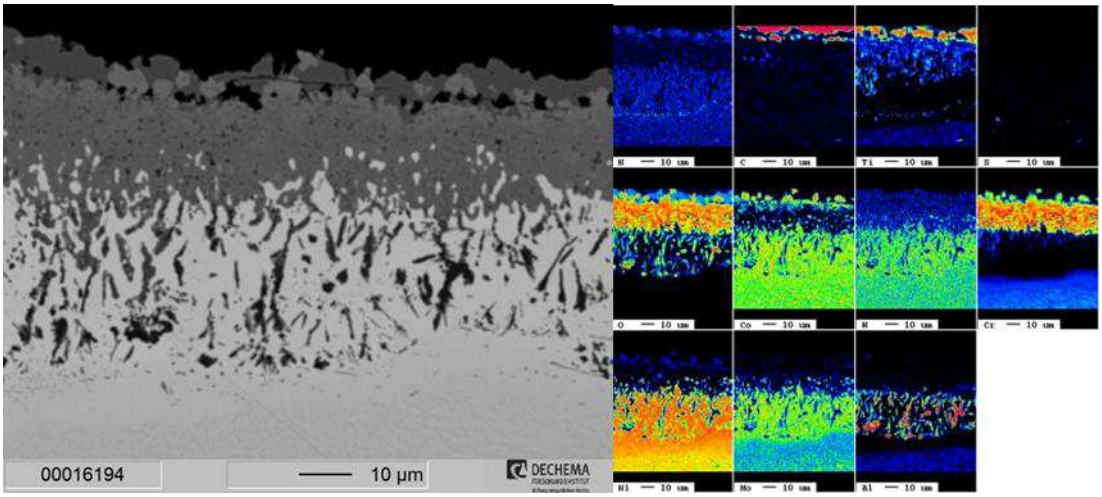

Figure 10: Cross-sectional BSE image and elemental distribution maps for Rene80 after hot corrosion with 20% water vapor at 900 °C for 1000 h.

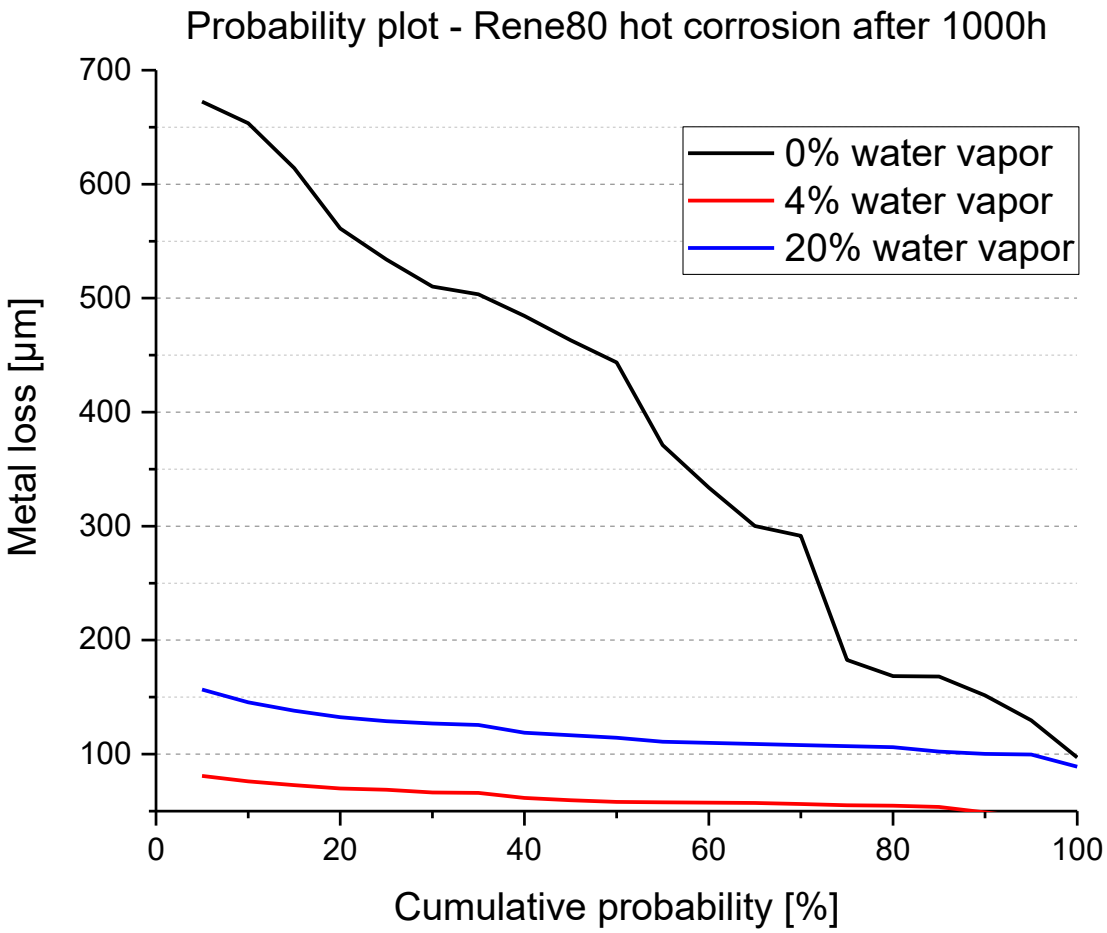

Figure 11: Cumulative probability plot for metal loss: Rene80 hot corrosion experiments with 0, 4 and 20% water vapor.

The microstructural trends are fully reflected in the cumulative probability plots of the remaining intact alloy cross-section, Figure 11. At 0 % H_2O, Rene 80 experiences the most severe degradation. The cumulative distribution shows extremely deep attack, with maximum penetration depths exceeding 600 µm. The median value indicates that 50 % of the measured cross-sections exhibit an attack depth of approximately 400 µm, confirming extensive and highly aggressive hot-corrosion damage. The addition of 4 % H_2O leads to a dramatic improvement. The cumulative distribution shifts sharply toward lower attack depths, no pitting is observed, and the median attack depth decreases to approximately 20 µm. This represents more than an order-of-magnitude reduction in effective material loss compared to the dry condition. At 20 % H_2O, the attack depth increases again relative to 4 % H_2O, although it remains far below the values observed at 0 % H_2O. The median attack is around 130 µm. There is no severe pitting observed. This indicates the presence of a water-vapor “sweet spot” for Rene 80, where corrosion suppression is maximized at intermediate H_2O levels.

The Rene 80 results demonstrate that water vapor introduces a non-monotonic influence on deposit-induced hot corrosion. In dry atmospheres, chromia destabilization and molybdate formation dominate, driving aggressive sulfidation and deep alloy penetration. The presence of Mo strongly amplifies this behavior, placing Rene 80 in a fully developed propagation regime of hot corrosion. Moderate water-vapor levels (4 %) fundamentally alter this regime. The suppression of molybdate formation, stabilization of chromia-rich oxide layers and strong reduction in sulfidation indicate that water vapor modifies the sulfate melt chemistry and interfacial equilibria in a way that inhibits Mo-assisted corrosion pathways. Under these conditions, oxide growth becomes diffusion-controlled rather than dissolution-driven. At higher water-vapor levels (20 %), oxide growth remains stabilized, but the altered surface morphology suggests changes in oxidation kinetics and transport processes.

The formation of discrete, rounded oxide regions points to a different balance between nucleation and lateral growth, potentially influenced by increased volatility of sulfate species or enhanced transport rates in the gas phase. As a result, corrosion resistance decreases slightly compared to the optimal condition at 4 % H_2O. Overall, Rene 80 benefits substantially from the presence of water vapor under deposit-induced hot-corrosion conditions, but exhibits an optimal H_2O concentration range beyond which further increases do not yield additional protection.

3.1.3 IN939

After 1000 h of exposure under deposit-induced hot-corrosion conditions, IN939 exhibits a corrosion response that is markedly different from CMSX-4 and Rene 80. The degradation behavior is dominated by its high chromium content, which stabilizes chromia-based protection [24,25] and seems to be even more beneficial at the investigated water-vapor levels, where it fully suppresses catastrophic hot-corrosion propagation.

IN939 at 0% H2O:

In the absence of water vapor, IN939 develops a well-defined, multi-layered oxide scale, Figure 12. Cross-sectional analysis reveals the formation of titanium nitrides and carbides within the near-surface region of the alloy. At the surface, an outer oxide layer consisting primarily of Ti-oxide with Ni-oxide is present. Beneath this layer, a thin Co-oxide zone is observed, followed by a thick, continuous chromium-rich oxide layer with a thickness of approximately 10 µm. WDX measurements show that this Cr-oxide layer remains largely intact and continuous, and—unlike in Rene 80—no complete chromium depletion zone develops beneath the scale. Sulfur ingress is limited, and sulfidation is minor compared to CMSX-4 and Rene 80. Beneath the chromia layer, internal, discontinuous Al-oxide is detected, indicating limited aluminum participation in scale formation but no establishment of a continuous alumina barrier. Overall, the corrosion morphology at 0 % H_2O indicates a chromia-dominated protection mechanism that effectively suppresses extensive sulfidation and deep internal attack, despite the presence of molten sulfate deposits.

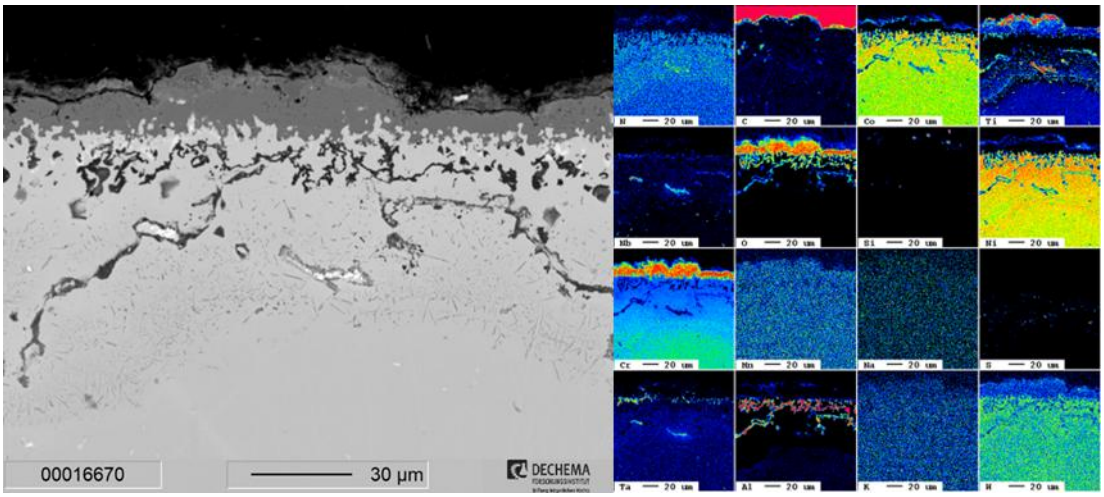

Figure 12: Cross-sectional BSE image and elemental distribution maps for IN939 after hot corrosion without water vapor at 900 °C for 1000 h.

IN939 at 4% H2O:

At 4 % H_2O, IN939 exhibits a corrosion morphology that is largely similar to that observed under dry conditions, Figure 13. Internal Ti-, Nb- and Ta-carbides are detected near the alloy surface, while the external oxide structure remains dominated by a continuous Cr-rich oxide layer. The presence of water

vapor does not significantly alter the oxide sequence or scale continuity. WDX maps confirm that chromium remains sufficiently available to sustain the chromia layer, and no extensive Cr-depleted zone develops. Sulfur penetration remains low, and no pronounced sulfidation fronts are observed. Thus, moderate water-vapor addition does not measurably enhance corrosion resistance in IN939 but also does not destabilize the chromia-based protection.

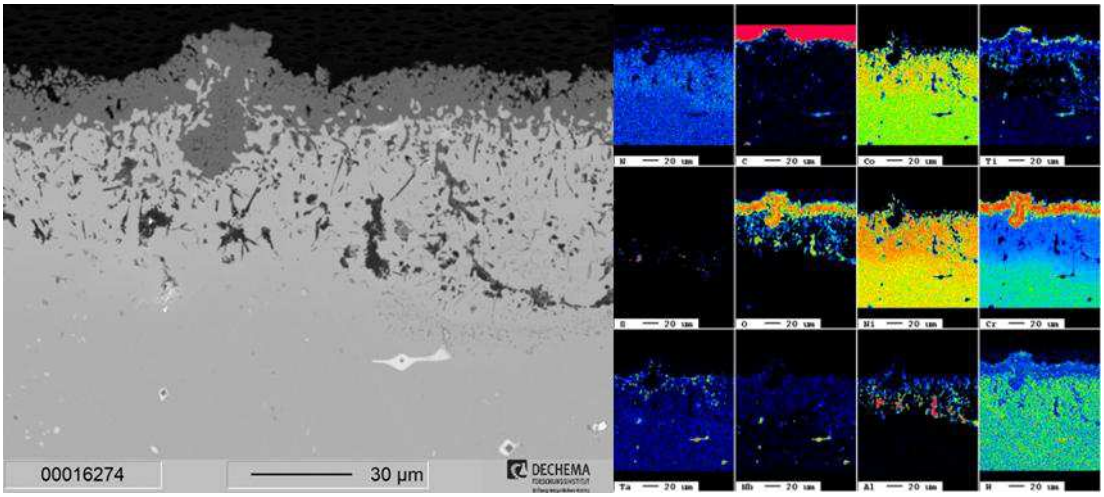

Figure 13: Cross-sectional BSE image and elemental distribution maps for IN939 after hot corrosion with 4% water vapor at 900 °C for 1000 h.

IN939 at 20% H2O:

At 20 % H_2O, the corrosion morphology remains essentially unchanged relative to the 4 % H_2O condition, Figure 14. The oxide scale continues to consist of an outer Ti/Ni-oxide, a thin Co-oxide region and a thick, continuous Cr-oxide layer. Carbide formation involving Ti, Nb and Ta persists, and internal Al-oxide remains discontinuous. No evidence of chromia breakdown, chromate-driven dissolution or extensive sulfidation is observed. The high water-vapor content therefore does not induce catastrophic degradation but also does not significantly improve the corrosion resistance beyond the level observed at lower H_2O contents.

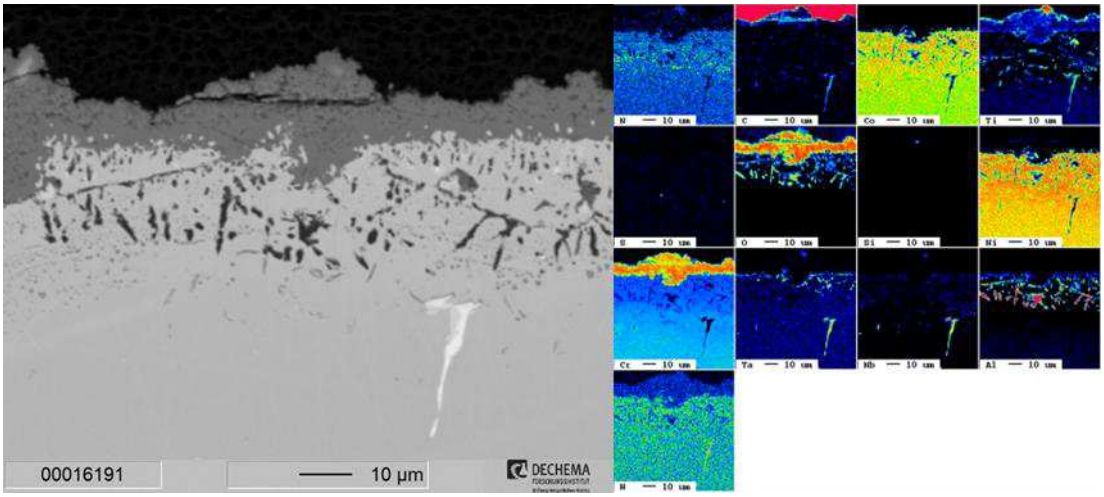

Figure 14: Cross-sectional BSE image and elemental distribution maps for IN939 after hot corrosion with 20% water vapor at 900 °C for 1000 h.

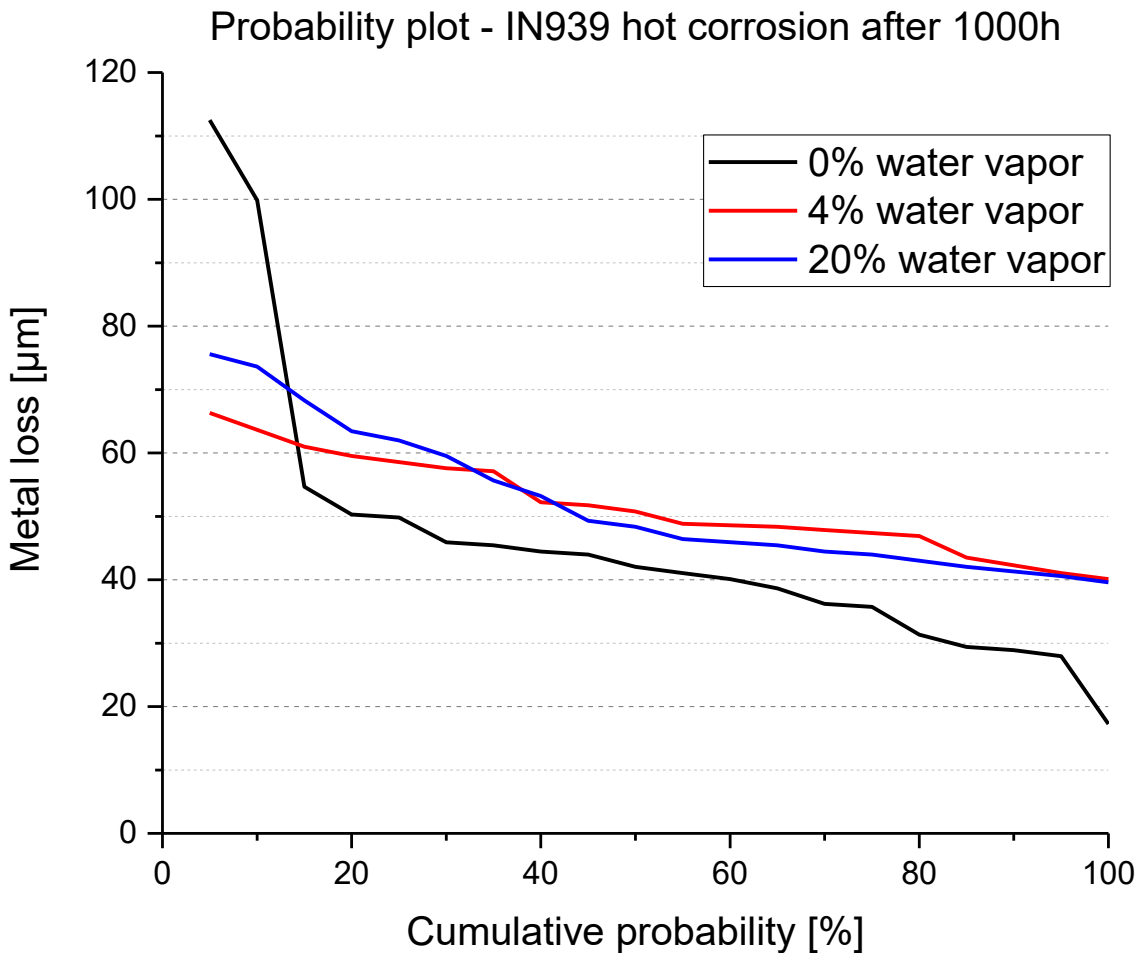

Figure 15: Cumulative probability plot for remaining intact metal: IN939 hot corrosion experiments with 0, 4 and 20% water vapor.

The cumulative probability plots of the remaining intact alloy cross-section, Figure 15, show that IN939 exhibits the most monotonic corrosion behavior among the three investigated alloys. At 0 % H_2O, IN939 shows the lowest median attack depth, with 50 % probability corresponding to approximately 42 µm. However, despite this favorable median, the cumulative distribution reveals the presence of localized pitting, beginning at probabilities below ~15 %. These pits exhibit attack depths ranging from approximately 55 µm up to 110 µm, representing the most severe localized damage observed for IN939 under all investigated conditions. At 4 % and 20 % H_2O, the cumulative distributions are very similar. Both conditions show median attack depths of approximately 50 µm, with maximum attack depths of about 65 µm (4 % H_2O) and 75 µm (20 % H_2O). Compared to the dry condition, localized extreme pitting is reduced, but the overall average attack is slightly higher. These results indicate that water vapor marginally homogenizes the corrosion attack in IN939 but does not significantly reduce the overall degradation depth.

The IN939 results highlight the dominant role of high chromium content in suppressing severe hot-corrosion propagation. Across all water-vapor levels, IN939 maintains a continuous chromia-based oxide scale, preventing extensive sulfidation and deep alloy penetration. WDX measurements confirm that chromium depletion remains limited, even after 1000 h. Unlike CMSX-4 and Rene 80, IN939 does not benefit substantially from the presence of water vapor. While moderate and high H_2O contents reduce localized extreme pitting, they do not lower the median attack depth. This behavior is attributed to the absence or limited effectiveness of high-stability oxide formers such as Aluminum, which in CMSX-4 and Rene 80 contribute to improved protection under humid conditions. Consequently, IN939 exhibits a corrosion response that is robust but comparatively insensitive to water-vapor-induced

changes in sulfate chemistry. The alloy avoids catastrophic degradation due to its chromia-dominated protection but does not achieve the low attack depths observed for CMSX-4 and Rene 80 under optimized water-vapor conditions.

3.2 Comparative assessment and alloy-specific attack (1000 h)

The combined microstructural analysis, WDX measurements and cumulative probability evaluation after 1000 h clearly demonstrate that the influence of water vapor on deposit-induced hot corrosion is strongly alloy dependent. While water vapor acts as a stabilizing parameter for some alloys, its effectiveness is governed by the balance between aluminum availability, chromium stability and the presence of additional reactive alloying elements.

CMSX 4 — Humidity stabilized alumina-controlled protection

Under dry conditions, CMSX 4 exhibits classical type I hot corrosion, characterized by deep pits and localized sulfidation and nitridation. The absence of humidity allows sulfate induced fluxing to destabilize protective alumina formation. In humid atmospheres, the corrosion mode changes fundamentally and CMSX-4 exhibits the strongest benefit of an increasing water-vapor content.

At high H_2O levels, the alloy forms a thin, homogeneous and compositionally stratified oxide scale, dominated by aluminum-rich oxides with minimal internal degradation. Sulfidation is effectively suppressed, internal nitridation is strongly reduced, and cumulative probability analysis confirms the lowest attack depths among all investigated conditions. This behavior indicates that water vapor promotes the stabilization of alumina-based protection in CMSX-4 under sulfate-covered conditions, despite the absence of a fully continuous bulk Al_2O_3 scale. The low chromium content limits chromate-related degradation pathways, allowing aluminum-controlled oxidation to dominate when sulfate aggressiveness is reduced by humid atmospheres.

Rene 80 — Humidity dependent suppression of Mo driven fluxing

Rene 80 shows a non-monotonic response to water vapor. In dry gas, the alloy undergoes alloy induced fluxing via molybdate formation, which destabilizes chromia and promotes internal Al and Ti depletion. This mechanism is characteristic of Mo containing superalloys under type I conditions. Moderate H_2O content (4 %) strongly suppresses hot corrosion, whereas higher H_2O levels lead to a partial increase in attack. In humid atmospheres, water vapor facilitates evaporation of MoO_3, reducing molybdate driven fluxing intensity. As a result, nitridation and sulfidation are significantly reduced at moderate humidity levels (≈4 %). At the elevated water-vapor contents of 20 %, the oxide scale consists of a non-protective, discontinuous alumina component combined with a thick, porous chromia layer, accompanied by internal aluminum depletion and localized sulfidation. The presence of molybdenum further amplifies corrosion susceptibility under unfavorable conditions by enabling molybdate formation when chromia is destabilized. As a result, Rene 80 exhibits an optimal water-vapor range in which oxide growth is stabilized, but it does not achieve the uniformly protective behavior observed for IN939.

IN939 — Chromia dominated stability with minimal humidity sensitivity

IN939 shows the lowest sensitivity to water vapor among the three alloys. Across all investigated H_2O levels, the corrosion attack remains relatively monotonic, with only minor variations in median attack depth. However, dry conditions still produced type I pits, but remarkably, even 4 % H_2O completely suppresses pit formation, resulting in a uniform chromia scale without catastrophic attack. WDX measurements reveal an even slightly thicker chromia scale when water vapour is present, effectively suppressing severe sulfidation and catastrophic attack. Generally, the high resistance is attributed to the alloy's high chromium and low aluminum content, which favors chromia-dominated protection and prevents the formation of stable alumina scales.

These results demonstrate that water vapor cannot be treated as a universally accelerating or mitigating factor in deposit-induced hot corrosion. Instead, its influence is strongly composition dependent:

4. Summary

- The influence of water vapor on deposit-induced hot corrosion at 900 °C is strongly dependent on alloy composition and cannot be described by a universal acceleration or mitigation effect.
- CMSX-4 exhibits a pronounced improvement in corrosion resistance with increasing water-vapor content, characterized by suppressed sulfidation, reduced nitridation and the formation of thin, homogeneous, aluminum-rich oxide scales at high H_2O levels.
- Rene 80 shows a complex response to water vapor, with maximum corrosion resistance at moderate H_2O content. While water vapor suppresses molybdate formation and chromia destabilization, porous chromia and non-protective alumina prevent long-term stabilization at higher humidity.
- IN939 remains largely insensitive to water vapor due to its high chromium and low aluminum content, maintaining a continuous chromia-based oxide scale with local pits only in dry conditions.
- These findings highlight the necessity of alloy-specific corrosion assessments when evaluating gas-turbine materials operating in humid, sulfur-containing environments.

5. Acknowledgements

References

[1] H. J. Maier, T. Niendorf and R. Bürgel, "Selection criteria for base elements and Overview of high-temperature material groups," in *Handbook of High-Temperature Materials Engineering*, Wiesbaden, Springer Vieweg, 2015, p. 322.

[2] R. Bürgel, "Festigkeit und Verformung der Metalle," in *Festigkeitslehre und Werkstoffmechanik Band 2*, Wiesbaden, Vieweg, 2005, pp. 1-89.

[3] "Klimaschutz Portal," Bundesverband der Deutschen Luftverkehrswirtschaft (BDL), [Online]. Available: https://www.bdl.aero/wp-content/uploads/2024/07/2020-klimaschutzreport-bdl.pdf. [Accessed 16 09 2025].

[4] A. Poullikkas, "An overview of current and future sustainable gas turbine technologies," *Renewable and Sustainable Energy Reviews,* vol. 9, pp. 409-443, 2005.

[5] J. Sumner, A. Potter, N. J. Simms and J. E. Oakey, "Modeling gas turbine materials' hot corrosion degradation in combustion environments from H2-rich syngas," *Materials and Corrosion,* vol. 68, no. 2, pp. 205-214, 2017.

[6] E. J. Oplia, "olatility of Common Protective Oxides in High-Temperature Water Vapor: Current Understanding and Unanswered Questions," *Trans Tech Publications,* Vols. 461-464, pp. 765-773, 2004.

[7] K. Onal, M. Maris-Sida, G. H. Meier and F. S. Petti, "The effects of water vapor on the oxidation of nickel-base superalloys and coatings at temperatures from 700°C to 1100°C," *Superalloys,* pp. 607-615, 2004.

[8] B. A. Pint, J. A. Haynes, Y. Zhang, K. L. More and I. G. Wright, "The Effect of Water Vapor on the Oxidation Behavior of Ni-Pt-Al Coatings and Alloys," *Surface and Coatings Technology,* vol. 201, pp. 3852-3856, 2006.

[9] M. Michalik, S. L. Tobing, M. Hänsel, V. Shemet, W. J. Quadakkers and D. Young, "Effects of water vapour on the high temperature nitridation of chromium," *Materials and Corrosion,* vol. 65, no. 3, pp. 260-266, 2013.

[10] G. H. Meier, "A Review of Advances in High-temperature Corrosion," *Materials Science and Engineering,* vol. AI20 , pp. 1-11, 1989.

[11] F. Pettit, "Hot Corrosion of Metals and Alloys," *Oxidation of Metals,* vol. 76, pp. 1-21, 2011.

[12] G. Meier, "Invited Review Paper in Commemoration of Over 50 Years of Oxidation of Metals: Current Aspects of Deposit-Induced Corrosion," *Oxidation of Metals,* vol. 98, pp. 1-41, 2022.

[13] Y. Wang, R. Pillai, E. Yazhenskikh, M. Frommherz and M. Müller, "Role of Temperature in Na 2SO 4–K 2SO 4 Deposit Induced Type II Hot Corrosion of NiAl Coating on a Commercial Ni-Based Superalloy," *Advanved Engineering Materials,* vol. 22, p. 1901244, 2020.

[14] P. Kotstad and G. Akesson, "Sultate-Induced High-Temperature Corrosion of Nickel," *Oxidation of Metals,* vol. 14, no. 4, pp. 301-323, 1980.

[15] B. S. Lutz, J. M. Alvarado-Orozco, L. Garcia-Fresnillo and G. H. Meier, "Na2SO4-Deposit-Induced Corrosion of Mo-Containing Alloya," *Oxidation of Metals,* vol. 88, pp. 599-620, 2017.

[16] L. Korell, K. Beck, A. R. Chitra, F. Hinrichs, C. Oskay, E. White, M. Heilmaier and M. C. Galetz, "Type II Hot Corrosion of Two Mo-Si-Ti Alloys and Mo-Si-B With a Salt Deposit of Mixed Na2 SO 4 and NiSO4," *Materials and Corrosion,* pp. 1-11, 2025.

[17] K. Beck, T. König, A. Case, C. Oskay and M. C. Galetz, "Hot Corrosion Behavior of Mo–9.0Si–8.0B," *Materials and Corrosion,* vol. 75, no. 12, p. 1600–1609, 2024.

[18] A. Potter, J. Sumner and N. Simms, "The effects of water vapour on the hot corrosion of gas turbine blade materials at 700 °C," *Materials at High Temperatures,* vol. 39, no. 3, pp. 231-238, 2022.

[19] J. R. Nicholls and D. J. Stephenson, "A life prediction model for coating based on the statistical analysis of hot salt corrosion performance," *Corrosion Science,* vol. 33, no. 8, pp. 1313-1325, 1992.

[20] M. Waeytens, A. U. Syed, T. Roberts, F. D. Martinez, S. Gray, J. Nicholls, Materials at High Temperatures 2023, 40, 272.

[21] H. Haight, A. Potter, J. Sumner, S. Gray, Oxid Met 2015, 84, 607.

[22] J. Sumner, A. Potter, N. J. Simms, J. E. Oakey, Materials at High Temperatures 2015, 32, 177.

[23] M. Kerbstadt, K. Ma, E. M. H. White, A. J. Knowles, M. C. Galetz, High Temperature Corrosion of mater. 2024, 101, 1077.

[24] M. Abedini, M. R. Jahangiri, P. Karimi, Oxid Met 2018, 90, 469.

[25] W. T. Wu, A. Rahmel, M. Schorr, Oxid. Met. 1983, 19, 201.